Article

Study on Temperature Field Distribution Law and Mechanical Properties of Hydraulic Tunnel-Surrounding Rock under the Action of Large Temperature Differences

Pengyuan Guan [1], Shuangxi Li [2], Haibo Jiang [1,2,*] and Pengfei Xiang [1,3]

1   College of Water Conservancy & Architectural Engineering, Shihezi University, Shihezi 832003, China; 20202110013@stu.shzu.edu.cn (P.G.); z20120190803@zjtongji.edu.cn (P.X.)
2   College of Hydraulic and Civil Engineering, Xinjiang Agriculture University, Urumqi 830052, China; xjlsx123@126.com
3   Department of Architectural Engineering, Zhejiang Tongji Vocational College of Science and Technology, Hangzhou 311200, China
*   Correspondence: klaud618@shzu.edu.cn

Abstract: This study aims to explore the temperature field and mechanical characteristics of hydraulic tunnels during operation in an area with large temperature differences throughout a year. By relying on the measured displacement field change results of a water transmission tunnel in Xinjiang, a finite element calculation model applicable to the hydraulic tunnel-surrounding rock under the action of large temperature differences was established. Then, the FEM model was used to analyze the temperature field distribution and stress field variation of hydraulic tunnel-surrounding rock under the effect of large temperature differences. The results showed that, under the action of large temperature differences, the displacement of the cave top was the largest, followed by the cave bottom, and finally the cave waist. The obtained displacement field data using the calculation model in this study were basically consistent with the on-site measured data, and the displacement field change law was the same, indicating that the established finite element calculation model is reliable. When the ambient temperature was below zero, the freezing front gradually expanded to the depth of the surrounding rock along the tunnel radial direction, while the frozen rock at the intersection of the lining and the surrounding rock melted first when the ambient temperature was above zero. The stress in various parts of the surrounding rock of the hydraulic tunnel increased continuously. To be specific, the growth rate of the tensile stress at the cave bottom, the tensile stress at the cave top, and the compressive stress at the cave waist of the tunnel reached 0.052 MPa/year, 0.053 MPa/year, and 0.096 MPa/year, respectively, in the first year, but the increasing rate subsequently tended to slow down continuously. Therefore, in actual projects, attention should be focused on the effect of large temperature differences on the stress growth of tunnel-surrounding rocks at an early stage, especially the growth of compressive stress at the cave waist. Notably, there are a large number of symmetrical and asymmetric phenomena related to engineering in this study.

Keywords: tunnel project; large temperature difference; displacement field; temperature field; stress field

1. Introduction

China's Xinjiang is located in a temperate continental climate region, where the temperature varies drastically within a year and the large temperature difference phenomenon is significant. The maximum large temperature difference throughout a year can be more than 65 °C, and sometimes the maximum large temperature difference during a day and night can be more than 30 °C. At present, many hydraulic tunnels in Xinjiang are under construction or have been completed. These hydraulic tunnels will experience four months of negative temperatures in winter, making the pore water inside the surrounding rock

freeze. Meanwhile, the unfrozen water will migrate to the edge of the positive freezing area, resulting in the continuous expansion of geotechnical volume and tunnel structure deformation. After the winter, the temperature rises and the ice rock melting will cause geotechnical deformation. When summer comes, the temperature continues to rise and the temperature stresses generated will have an impact on the surrounding rock deformation. Exploring the temperature field distribution law and the mechanical properties of the hydraulic tunnel-surrounding rock under the action of large temperature differences is of great significance to the protection of hydraulic tunnels in Xinjiang.

At present, for the frost-heaving problem of hydraulic tunnel-surrounding rock at low temperatures and the strain force of the surrounding rock at high temperatures, some scholars have conducted certain studies through model tests [1–8], theoretical calculations [9–13], finite element simulations [14–24], etc. Regarding the freezing and thawing of the surrounding rock at low temperatures, Konrad et al. [1] carried out experiments to show that, in addition to the frozen part and the unfrozen part in the frozen rock, there is a freezing front between the two. Yu et al. [2] used semi-empirical models to study the stress characteristics of the lining of non-circular shallow tunnels under freeze–thaw action, and found that the freezing and expansion pressure on the sidewall occurred earliest. Zhang et al. [3] evaluated the comprehensive effects of freeze–thaw cycles, salt content, confining pressure, and strain rates on strength through the triaxial compression test with fixed drainage. Xu et al. [4] conducted a series of non-saturated concrete tests to explore the deterioration of concrete under different freeze–thaw cycles, and the research results provided rich implications for the study of freeze–thaw cycles in cold region tunnels. Nakano et al. [9] mathematically studied the stable movement process of frozen soil in the freezing front region based on the assumption of freezing edge characteristics. Gatmiri et al. [10] derived the THM coupling mathematical equation for low-temperature rock freezing. Zhu et al. [11] derived a mechanical model for calculating frost heave pressure and frost heave deformation based on the constant stiffness constraint model of rock and the frost heave strain model. Deng et al. [14] proposed a frost heave prediction method based on the cold expansion coefficient to simulate the deformation of the foundation of Gongbei Tunnel. Bonacina et al. [15] proposed a numerical solution for the temperature field by taking into account the effect of phase change on heat conduction. Zhang et al. [16] proposed an improved ordinary state-based peridynamic (OSBPD) model to study the freeze–thaw cycles in tunnels in cold regions. Regarding the stress–strain problem of the surrounding rock at high temperatures, the laboratory experimental results of Yao et al. [7] showed that the high-temperature water flow in tunnels causes temperature differences between the inner and outer walls of the supporting structures, resulting in higher circumferential tensile stresses in the supporting structures of high-temperature hydraulic tunnels. Liu et al. [12] studied the distribution patterns of temperature fields and stress fields in high-temperature tunnels under the combined action of gravitational stress and temperature stress when temperature stabilizes. Hao et al. [20] combined the extended finite element method and established a numerical analysis model for temperature, humidity, and stress multi-factor coupling. Zhao et al. [21] studied the effects of mechanical ventilation parameters and insulation layer thickness on the temperature of the tunnel-surrounding rock in the planned Zheduo mountain Tunnel. Zeng et al. [22] studied the effects of ventilation frequency and velocity on the environmental temperature inside the tunnel through numerical simulations. Focusing on the impact of large temperature differences on different engineering structures, Liu et al. [25] analyzed the meteorological characteristics of regions with large temperature differences throughout a year and conducted a systematic study on the differences in the structural behavior between concrete arch dams in high-cold areas and mild-climate regions. Zhang et al. [26] introduced different construction methods for the concrete lining of channel slopes under large temperature difference conditions, in order to improve the compactness of the lining concrete, increase the carrying capacity of the channel, and improve the water utilization coefficient of the channel. The results of previous scholars' studies show that when the ambient temperature is below zero, the

surrounding rock will generate frost heaving force, and its frost heave is related to the temperature, moisture, and frost heaving sensitivity of the surrounding rock; when the frozen rock melts, the rock and soil body particle skeleton that loses the support of the frost heaving force will generate a certain amount of deformation, and the surrounding rock will undergo deterioration damage and freeze–thaw damage under multiple freeze–thaw cycles; in the high temperature environment, the surrounding rock will generate a large stress–strain, which affects the stability of the surrounding rock. So far, most studies have mainly focused on single studies of the freeze-heave, freeze–thaw process or high temperatures; however, the actual ambient temperature in large temperature difference areas throughout a year shows cyclic changes. There are few studies on the changes of hydraulic tunnel-surrounding rocks from freeze-heaving action to freeze–thaw action, and to high temperature action, so it is necessary to conduct further research.

In this paper, based on a hydraulic tunnel project in Xinjiang, the ambient temperature monitoring and displacement monitoring were carried out throughout a year to analyze the deformation distribution law of the tunnel-surrounding rock under the action of a large temperature difference. A finite element calculation model applicable to the tunnel-surrounding rock under the action of large temperature differences was established. Then, the temperature field distribution and mechanical characteristics of the tunnel-surrounding rock under large temperature differences were analyzed by finite element calculation. This can provide a better understanding for the construction of hydraulic tunnels in areas with large temperature differences during a year. In addition, the study on temperature field distribution law and the mechanical properties of hydraulic tunnel-surrounding rock under the action of large temperature differences has revealed many symmetrical phenomena.

2. Engineering Measurement Analysis

2.1. Project Overview

The studied hydraulic tunnel in Xinjiang has a total length of about 1525.2 m and an elevation of 1672.0 m at the cave top. It shows a rounded cavity shape in the pressurized cavern section, and the lithology is mainly tuff and dolomitic tuff. Geological analysis shows that the overall geological structure of the tunnel is stable, but there are small cracks in the exit section, which can be roughly divided into two groups: $330°\sim350°$ SW$\angle30°\sim40°$ and $300°\sim330°$ SW$\angle70°\sim80°$. The cracks are flat, sealed, and unfilled. The tunnel is located in a slightly weathered rock mass, and the surrounding rock belongs to Class III. The extreme minimum temperature is $-24.6\ °C$ and the extreme maximum temperature is $41.1\ °C$ throughout a year. The large temperature difference during the year has an adverse effect on the working state of the tunnel, so measures need to be taken to reduce safety risks during operation. The relevant parameters of the surrounding rock and lining in this project are shown in Tables 1–3. The location of the hydraulic tunnel is shown in Figure 1.

Table 1. Physical parameters.

Material	Density/(kg·m^{-3})	Elastic Modulus/GPa	Poisson's Ratio	Cohesion/MPa	Internal Friction Angle/(°)
Surrounding Rock	2300	3.5	0.29	1.3	42
Lining	2500	30	0.2		

Table 2. Thermal parameters.

Material	Specific Heat Capacity/(kJ·kg^{-1}·°C^{-1})	Thermal Conductivity /(W·m^{-1}·C^{-1})	Density/(kg·m^{-3})
Surrounding Rock	0.89	1.38	2300
Lining	0.97	1.58	2500
Water	4.20	0.63	1000
Ice	2.10	2.31	918

Table 3. Hydraulics parameters.

Material	b_0	m	f	Permeability Coefficient/(m·s^{-1})	Saturated Water Content
Surrounding Rock	2	0.5	0.5	9.62×10^{-6}	0.25
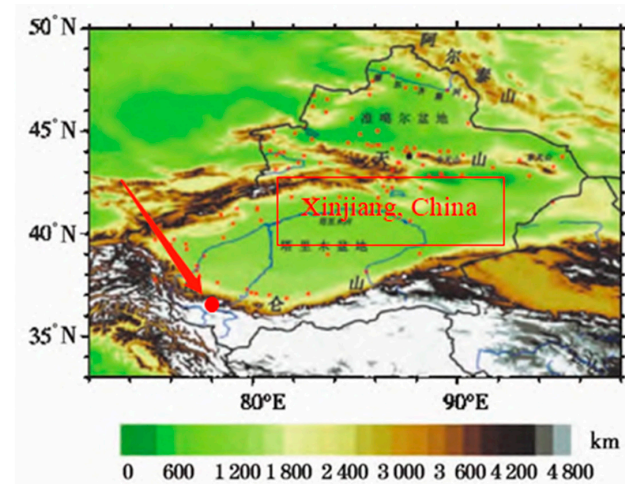
Figure 1. Location of the tunnel.

2.2. On-Site Monitoring Scheme for the Hydraulic Tunnel under Large Temperature Difference

The local climate and engineering geological conditions were considered to study the deformation of tunnel-surrounding rock caused by temperature changes in hydraulic tunnels under the effect of large temperature differences with seasonal and periodic changes within a year. On-site displacement monitoring and temperature monitoring were adopted to reveal the relationship between the surrounding rock displacement and the temperature of the hydraulic tunnel. Finally, the bearing characteristics of the surrounding rock were analyzed, which can provide a reference for the safety of hydraulic tunnels.

The monitoring points were arranged according to the actual situation of the hydraulic tunnel site. Five sets of four-point displacement meters (BGK-A3, Beijing Jikang Technology), with an accuracy of 0.01 mm, were used for monitoring the surrounding rock displacement data. The displacement meters were arranged at elevations of 1672.0 m, 1678.0 m, 1685.0 m, and 1711.0 m above the tunnel, respectively. They were buried by grouting after drilling, and were read every 25 days. The on-site monitoring layout is shown in Figure 2.
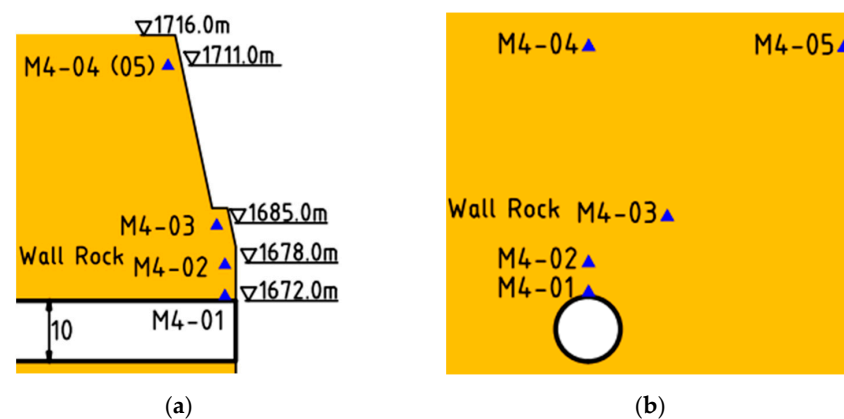
Figure 2. Layout of monitoring instrument. (**a**) Sectional view of monitoring instrument layout. (**b**) Elevation view of monitoring instrument layout.

2.3. Analysis of Monitoring Results

According to the monitoring results, the displacement monitoring data of each monitoring point for 1 year after the completion of the tunnel project were analyzed, and the monitoring results of different measuring points are shown in Figure 3. The displacement direction of the surrounding rock above the tunnel is vertical downwards.
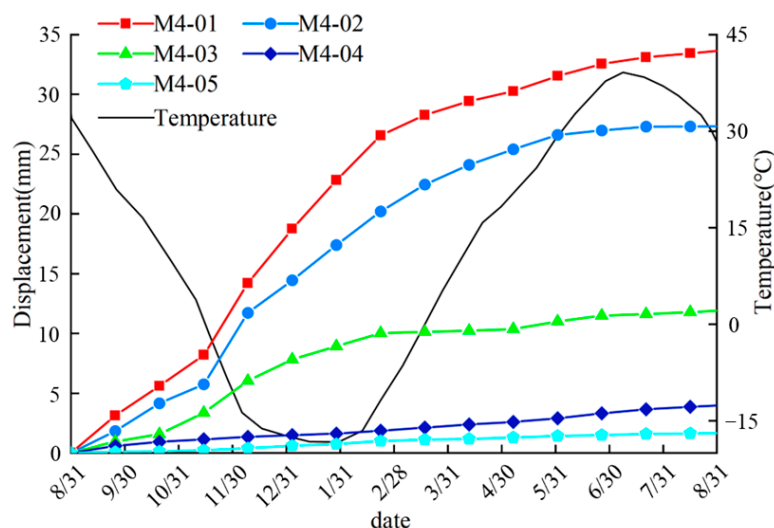

Figure 3. Displacement monitoring value of each point and ambient temperature monitoring value.

According to the comparison of tunnel-surrounding rock displacements in different positions, as shown in Figure 3, the following can be obtained:

(1) The three points, M4-01, M4-02, and M4-04, are located directly above the tunnel, among which, point M4-01 is the top position and is the closest to the tunnel, and point M4-04 is the farthest from the tunnel. At the same moment, the differences in the displacement sizes of the three points can be clearly seen, and the displacement sizes are ordered as M4-01 > M4-02 > M4-04. After one year from the start of the monitored readings, the displacement of point M4-01 was 33.6 mm with an average rate of displacement change of 0.092 mm/d; the displacement of point M4-02 was 27.3 mm with an average rate of displacement change of 0.075 mm/d; and the displacement of point M4-04 was 3.8 mm with an average rate of displacement change of 0.011 mm/d.

(2) The three points, M4-01, M4-03, and M4-05, are connected to a straight line at an angle of 45° to the plumb line, where point M4-01 is the closest to the tunnel and point M4-05 is the farthest from the tunnel. At the same moment, the displacement sizes of these three points are obviously different, and the displacement sizes are ordered as M4-01 > M4-03 > M4-05. From the start of the monitored readings to one year later, the displacement of point M4-03 was 11.9 mm, with an average displacement change rate of 0.033 mm/d, and the displacement of point M4-05 was 1.7 mm, with an average displacement change rate of 0.005 mm/d.

(3) The two points, M4-04 and M4-05, are on the same horizontal line, where M4-04 is directly above the tunnel and M4-05 is diagonally above the tunnel and deviates from the plumb line by 45°. At the same moment, the displacement sizes of these two points are different, and the displacement sizes are ordered as M4-04 > M4-05.

According to the analysis of the evolution of the tunnel-surrounding rock displacement with time, as shown in Figure 3, the following can be obtained:

(1) During days 0~80, the ambient temperature decreased from 23.8 °C to 0 °C, and the displacement changes of the five points from M4-01 to M4-05 during this period were 9.3 mm, 6.9 mm, 3.9 mm, 1.2 mm, and 0.6 mm; the change rates of displacement were 0.116 mm/d, 0.086 mm/d, 0.049 mm/d, 0.015 mm/d, and 0.008 mm/d, respectively.

(2) During days 81~190, the ambient temperature decreased from 0 °C to −18.5 °C and then rose back to 0 °C. During this period, the displacement changes of the five points from

M4-01 to M4-05 were 18.3 mm, 14.7 mm, 6.2 mm, 0.9 mm, and 0.5 mm; the change rates of displacement were 0.166 mm/d, 0.134 mm/d, 0.056 mm/d, 0.008 mm/d, and 0.005 mm/d, respectively. Comparing the displacement change rates during days 0~80, the displacement change rates of the three points, M4-01, M4-02, and M4-03, increased during days 81~190, while the displacement change rate of the two points, M4-04 and M4-05, decreased. The consideration from the perspective of temperature is mainly because when the ambient temperature was lower than 0 °C, the three points, M4-01, M4-02, and M4-03, which are closer to the tunnel, resulted in frost heave deformation. Due to the two points M4-04 and M4-05, being far away from the tunnel, they were almost not affected by the frost heave deformation. In addition, with the consolidation of the surrounding rock, the deformation rate of the surrounding rock was reduced with time.

(3) During days 191~365, the ambient temperature increased from 0 °C to 39.1 °C and then decreased to 19.3 °C. During this period, the displacement changes of the five points, M4-01~M4-05, were 6 mm, 5.7 mm, 1.8 mm, 1.7 mm, and 0.6 mm, and the displacement change rates were 0.034 mm/d, 0.033 mm/d, 0.01 mm/d, 0.01 mm/d, and 0.003 mm/d, respectively. Compared with the two periods of days 0~80 and days 81~190, the displacement change rates of the five points, M4-01~M4-05, during days 191~365 were the slowest. This is mainly because of the further reduction in the displacement change rate of the surrounding rock caused by the consolidation of the surrounding rock.

3. Finite Element Calculation Model

In order to further analyze the temperature field distribution law and mechanical characteristics of hydraulic tunnel-surrounding rock under the action of large temperature differences, a finite element calculation model applicable to hydraulic tunnel-surrounding rock under the action of large temperature differences was established. Because of unsaturated seepage in the surrounding rock, the pores of the surrounding rock are not full of water. This simulation mainly considers the water flow field in the surrounding rock to reflect the frost heave deformation of the surrounding rock and the migration of liquid water to the freezing front at low temperatures.

3.1. Basic Assumptions

The surrounding rock is homogeneous, continuous, and isotropic. In an actual engineering situation, due to the impact of cracks, the moisture within the calculation boundary range does not exchange with the outside world during the entire calculation process. The fracture width is negligible, and heat transfer and pore water seepage are not affected by fractures.

3.2. Governing Equations and Their Applications

3.2.1. Temperature Field Governing Equation

According to Fourier's law, the heat conduction equation of the water–ice phase transition caused by the temperature of the surrounding rock falling below zero is considered [27]:

$$\rho C(\theta)\frac{\partial T}{\partial t} = \lambda(\theta)\nabla^2 T + L \cdot \rho_i \frac{\partial \theta_i}{\partial t} \tag{1}$$

where ρ is the density of the surrounding rock (kg/m^3); C is the heat capacity of the surrounding rock (J/(kg·°C)); T is temperature (°C); t is time (s); λ is the thermal conductivity (W/(m·°C)); L is the latent heat of the phase change, which is 334.5 kJ/kg; ρ_i is the density of ice (kg/m^3); and ∇ is the Hamiltonian.

When studying the effect of moisture on heat conduction, not only the pore water in the surrounding rock but also the ice content in the pores should be considered, so that the expression of the volumetric water content is [28]:

$$\theta = \theta_u + \rho_i/\rho_w \cdot \theta_i \tag{2}$$

where θ_u is the volume content of unfrozen water; θ_i is the volume ice content; and ρ_w is the density of water (kg/m^3).

In addition, the heat conduction equation in the lining is [27]:

$$\rho_c C_c \frac{\partial T}{\partial t} = \lambda_c \nabla^2 T \tag{3}$$

where ρ_c is the density of the lining (kg/m^3); C_c is the heat capacity of the lining (J/(kg·°C)); and λ_c is the thermal conductivity of the lining (W/(m·°C)).

3.2.2. Moisture Field Governing Equation

The water–ice phase transition is the main factor affecting moisture migration, so the water–ice phase transition term is added to the unsaturated seepage motion equation to obtain the Richards equation containing the water–ice phase transition [29]:

$$\frac{\partial \theta_u}{\partial t} + \frac{\rho_i}{\rho_w} \frac{\partial \theta_i}{\partial t} = \nabla[D(\theta_u)\nabla\theta_u + k(\theta_u)] \tag{4}$$

where k is the permeability coefficient of the surrounding rock.

The diffusion rate of the water in the surrounding rock can be calculated using the following equation [29]:

$$D(\theta_u) = \frac{k(\theta_u)}{c(\theta_u)} \cdot I \tag{5}$$

where $k(\theta_u)$ is the permeability (m/s); $c(\theta_u)$ is the specific water capacity (1/m); and I is the impedance factor, which means the strength of the ice to moisture migration.

$k(\theta_u)$ is calculated as follows:

$$k(\theta_u) = k_s \cdot S^f(1 - (1 - S^{1/m})^m)^2 \tag{6}$$

$c(\theta_u)$ is calculated as follows:

$$c(\theta_u) = b_0 m/(1 - m) \cdot S^{1/m}(1 - S^{1/m})^m \tag{7}$$

I is calculated as follows [30]:

$$I = 10^{-10\theta_i} \tag{8}$$

where b_0, m, and f are VG model parameters related to the surrounding rock; k_s is the permeability coefficient of saturated rock mass (m/s); and S is the relative saturation.

S is calculated as follows:

$$S = \frac{\theta_u - \theta_r}{\theta_s - \theta_r} \tag{9}$$

where θ_r is the residual water content; θ_s is the saturated water content.

In order to simultaneously solve the governing equation of the temperature field and the governing equation of the moisture field, a coupling term needs to be added. The solid–liquid ratio B_I is selected as the coupling term, which is the volume ratio of ice to water in the surrounding rock, and can be calculated as follows [28]:

$$B_I = \frac{\theta_i}{\theta_u}\begin{cases} 1.1(\frac{T}{T_f})^B - 1 & T < T_f \\ 0 & T \geq T_f \end{cases} \tag{10}$$

where T_f is the freezing temperature of the surrounding rock (°C); B is a parameter related to the salt content of the surrounding rock.

Equations (1), (3), (4), and (10) are to calculate the temperature field, moisture field, and lining temperature field of the surrounding rock. This equation group accurately expresses the effect of temperature changes on pore water motion and phase transition. The migration and phase transition of moisture cause changes in thermal conductivity;

temperature changes lead to changes in the volume content of water and ice during the water–ice phase transition, and the heat absorbed or released by the phase transition latent heat affects the temperature field distribution of the surrounding rock.

3.2.3. Stress Field Governing Equations

Equilibrium equation:

$$-\nabla \cdot \sigma = F \tag{11}$$

where F is the volume force component; σ is the stress.

Geometric equation:

$$\varepsilon = \nabla u \tag{12}$$

where u is the displacement component; ε is the strain.

Constitutive model:

$$\{\sigma\} = [c](\{\varepsilon\} - \{\varepsilon_0\}) \tag{13}$$

where $[c]$ is a constant matrix.

The strain of tunnel-surrounding rock under the action of large temperature differences includes transient strain, the strain caused by temperature change, and the strain caused by the water–ice phase transition and moisture migration:

$$\varepsilon = \varepsilon^e + \varepsilon_i + \varepsilon_v \tag{14}$$

where ε^e is the transient strain; ε_i is the strain caused by temperature change; and ε_v is the strain caused by the water–ice phase transition and moisture migration.

The strain caused by temperature change can be expressed as follows:

$$\varepsilon_i = \alpha(T - T_0) \tag{15}$$

where α is the linear expansion coefficient of the surrounding rock; T is the instantaneous temperature (°C); and T_0 is the initial temperature (°C).

The strain induced by the water–ice phase transition and moisture migration can be expressed as follows:

$$\varepsilon_v = (\rho_w/\rho_i - 1) \cdot \theta_s(S - S_0) \tag{16}$$

3.2.4. Simulation Method

The COMSOL Multi-physics finite element software can efficiently and quickly calculate multi-physics coupling and nonlinear differential equations. In this paper, the PDE interface in the software was used to define the variables and parameters related to the governing equations, and the coefficients of the assumed equations already in the software were used as inputs to solve the governing equations. This paper brings in the elastoplastic theory, which assumes that the rock mass is an elastoplastic material that meets the general assumption of elastoplasticity. Both the surrounding rock and the lining obey the Mohr–Coulumb yield criterion. First, the stress equilibrium after tunnel excavation is performed, and then the equilibrium ground stress is introduced as an initial condition into the stress field of the multi-physics coupling calculation for a transient solution.

3.3. Geometric Model Dimensions, Boundary Constraints, and Meshing

Based on the actual engineering situation, the section at a depth of 15 m from the tunnel exit was selected as the calculation section. The boundary range for calculation was taken as 3 to 5 times the tunnel diameter to reduce the interference of boundary effects. Due to the cross-sectional dimensions of the tunnel being much smaller than the tunnel length, the geometric model was simplified to a two-dimensional plane problem. The circular hydraulic tunnel was left–right symmetrical, and half of the tunnel cross-section was used as the finite element calculation area. Therefore, the geometric model size was determined as 34 m × 68 m. The boundary conditions are as follows: an applied downward stress of

0.345 MPa to the upper boundary, a fixed constraint on the lower boundary, a symmetric constraint on the left boundary, and a roller support constraint on the right boundary. The mesh division and geometric model are shown in Figure 4.
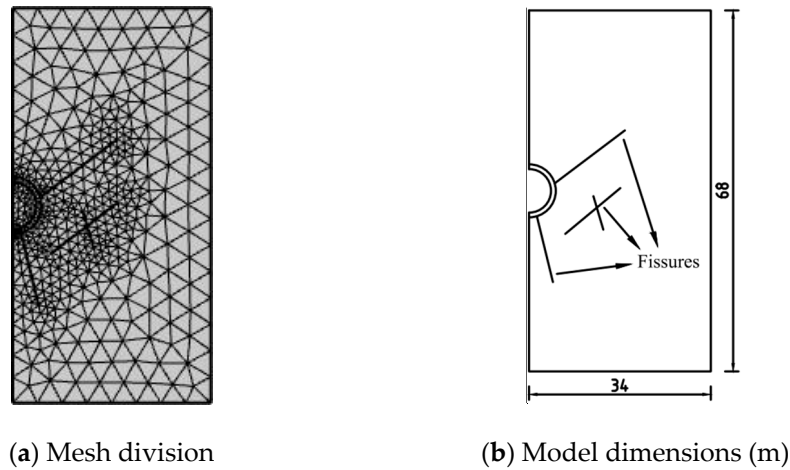

(**a**) Mesh division   (**b**) Model dimensions (m)

Figure 4. Geometry and mesh division.

3.4. Initial and Boundary Conditions of Surrounding Rock Temperature

The initial temperature of the surrounding rock in the radial depth of the tunnel is less influenced by the ambient temperature and remains at a low value with little fluctuation throughout the year. According to the site monitoring data, the initial value of the surrounding rock temperature field was set to 2 °C. The temperature throughout a year usually changes periodically and regularly with time, and therefore, the relationship between temperature and time was fitted as a sinusoidal function and used as a boundary condition of hydraulic tunnel temperatures under the effect of large temperature differences. The fitted equation is shown in Equation (17):

$$T = 11.12 + 29.8 \times \sin(\pi \times (t - 252.99)/182.5) \qquad (17)$$

where T is the temperature of the day (°C); t is the time (d).

3.5. Model Parameter Selection

The required parameters mainly include the model-calculated physical parameters and the model thermal parameters, whose magnitudes are shown in Tables 1–3. In addition, the latent heat of the phase change is 334.56 kJ/kg, and the initial saturation is 0.85.

4. Calculation Result Analysis

4.1. Displacement Field Verification

Figure 5 shows the distribution of the surrounding rock displacement field of the hydraulic tunnel under the action of large temperature differences after the completion of tunnel excavation. Figure 6 compares the on-site monitoring results and the numerical calculation results of the surrounding rock displacement.

An analysis of the displacement field of the surrounding rock in Figure 5 shows that the displacement at the top, bottom, and waist of the tunnel increased in one year under different combinations of gravity, frost heave, temperature stress, and overlying geotechnical pressure. The displacements of different parts of the tunnel after one year of large temperature differences are ordered as cave top > cave bottom > cave waist, and the displacement sizes are 33.43 mm, 13.46 mm and 11.81 mm, respectively. From Figures 3 and 5, it can be seen that above the cave top, the displacement becomes smaller as it draws closer to the depth of the surrounding rock, and the displacement distribution law of the simulation is the same as that of the actual measured data.
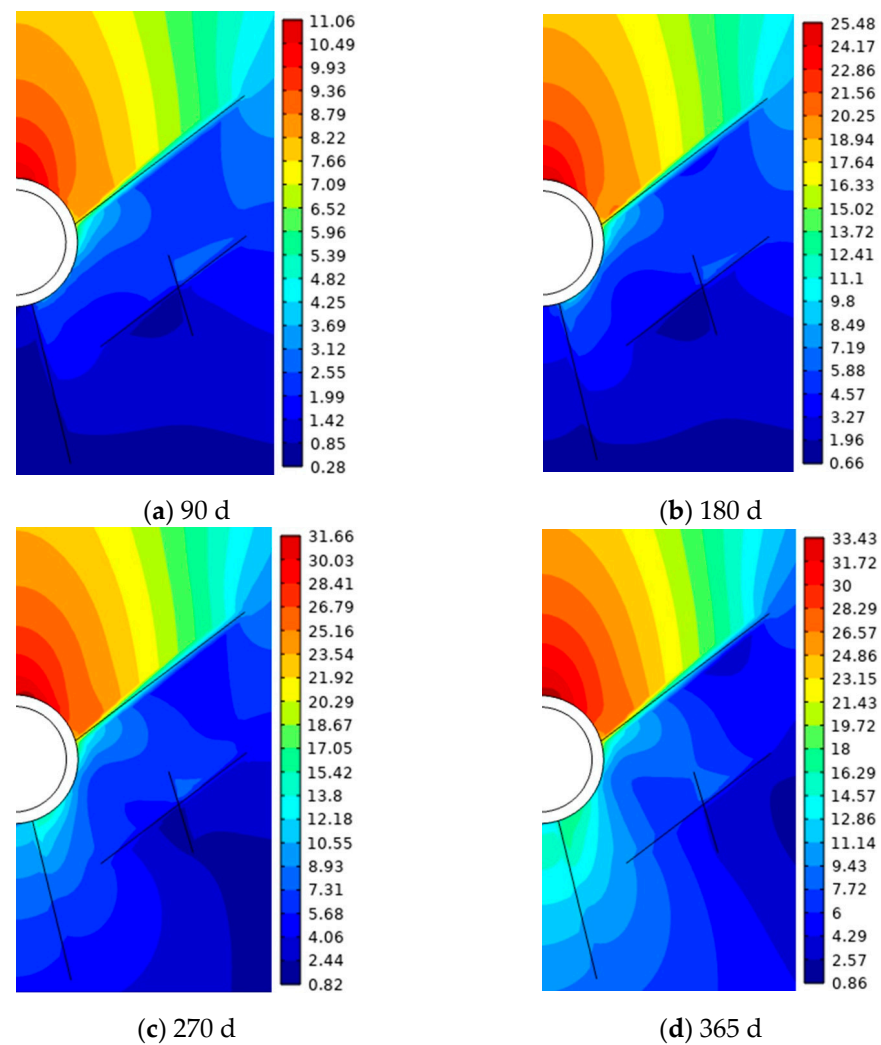
(**a**) 90 d

(**b**) 180 d

(**c**) 270 d

(**d**) 365 d

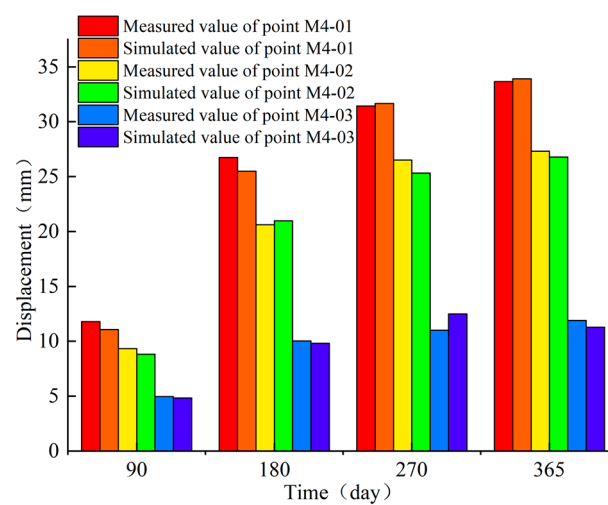**Figure 5.** Cloud chart of displacement field distribution of surrounding rocks (mm).

Figure 6. Comparison of field monitoring results and numerical calculation results of surrounding rock displacement.

The Mann–Whitney U test is a non-parametric test method, which is applicable to the comparison of two independent samples. In the comparative displacement analysis, the monitored and numerically calculated values of the tunnel-surrounding rock displacement

are two independent samples, so the Mann–Whitney U test can be used to compare whether there is a significant difference between these two sets of data in Figure 6, the surrounding rock field monitoring and the numerical simulation.

Since the three monitoring points, M4-01, M4-02, and M4-03, are close to the tunnel entrance, the displacement is large, and their displacement changes show obvious patterns under the action of large temperature differences. Therefore, the numerical calculated displacement values of these three points were extracted and compared with the actual measured values in the field. The time points were selected as the 90th day, the 180th day, the 270th day, and the 365th day. The calculation process of the Mann–Whitney U test is as follows [31]:

(1) Calculate the rank sum of each sample Σr_i:

The rank is actually the ordinal number, and the rank sum is the result of adding up each ordinal number in a set of data.

(2) Calculate the U-value [31]:

$$U_1 = n_1 \cdot n_2 + \frac{n_1 \cdot (n_1 + 1)}{2} - \sum_{i=1}^{n_1} r_{i1} \tag{18}$$

$$U_2 = n_1 \cdot n_2 + \frac{n_2 \cdot (n_2 + 1)}{2} - \sum_{i=1}^{n_2} r_{i2} \tag{19}$$

where n_1 and n_2 are the sample capacities of the measured and simulated values, respectively; r_{i1} and r_{i2} are the i values of the measured and simulated values in order of the i-th value in the order of size.

The number of small and medium U_1, U_2 is taken to be equal to U.

(3) Pick the significance level α and calculate the critical value U(α) based on the sample sizes n_1 and n_2:

According to the sample size and significance level, the U-value table of the Mann–Whitney U test can be found, and the corresponding critical value U(α) can be found. In this paper, the number of samples per group of data $n_1 = n_2 = 4$, the significance level $\alpha = 0.05$, and the critical value U(0.05) = 0 can be obtained according to the U-value table.

(4) Compare the calculated U-value with the critical value U(α):

If the U value is greater than or equal to the critical value U(α), the two sets of data are considered not significantly different, i.e., the difference between the numerical simulation results and the field monitoring results is not significant. Otherwise, it is considered that there is no significant difference between the two sets of data, i.e., the numerical simulation results are different from the field monitoring results.

The results of the Mann–Whitney U test calculations are shown in Table 4:

Table 4. Mann–Whitney U test calculation results.

	M4-01				M4-02				M4-03			
	Measurement	r_i	Simulation	r_i	Measurement	r_i	Simulation	r_i	Measurement	r_i	Simulation	r_i
90 d	11.79	2	11.06	1	9.33	2	8.82	1	4.962	2	4.83	1
180 d	26.75	4	25.48	3	20.61	3	20.98	4	10.03	4	9.81	3
270 d	31.42	5	31.66	6	26.51	6	25.33	5	11.01	5	12.48	6
365 d	33.65	7	33.91	8	27.31	8	26.79	7	11.9	8	11.28	7
Σr_i	-	18	-	18	-	19	-	17	-	19	-	17
U		8				7				7		
U(α)		0				0				0		

Through the Mann–Whitney U test, it can be concluded that the difference between the field monitoring and numerical calculation values of the tunnel-surrounding rock displacement is small, and the accuracy of the numerical simulation is also verified by the comparison of the surrounding rock displacement results.

4.2. Temperature Field Analysis

The development of the surrounding rock temperature field during the 365-day temperature conduction process under cyclic changes in ambient temperature is shown in Figure 7. The temperature variation curves with time inside the tunnel and at different radial depths in the surrounding rock are shown in Figure 8. The surrounding rock begins to freeze as the ambient temperature drops below zero. As time goes on, the ambient temperature rises above zero and the frozen rock begins to thaw. The change process of the frozen circle of the surrounding rock is shown in Figure 9.

(**a**) 90 d

(**b**) 180 d

(**c**) 270 d

(**d**) 365 d
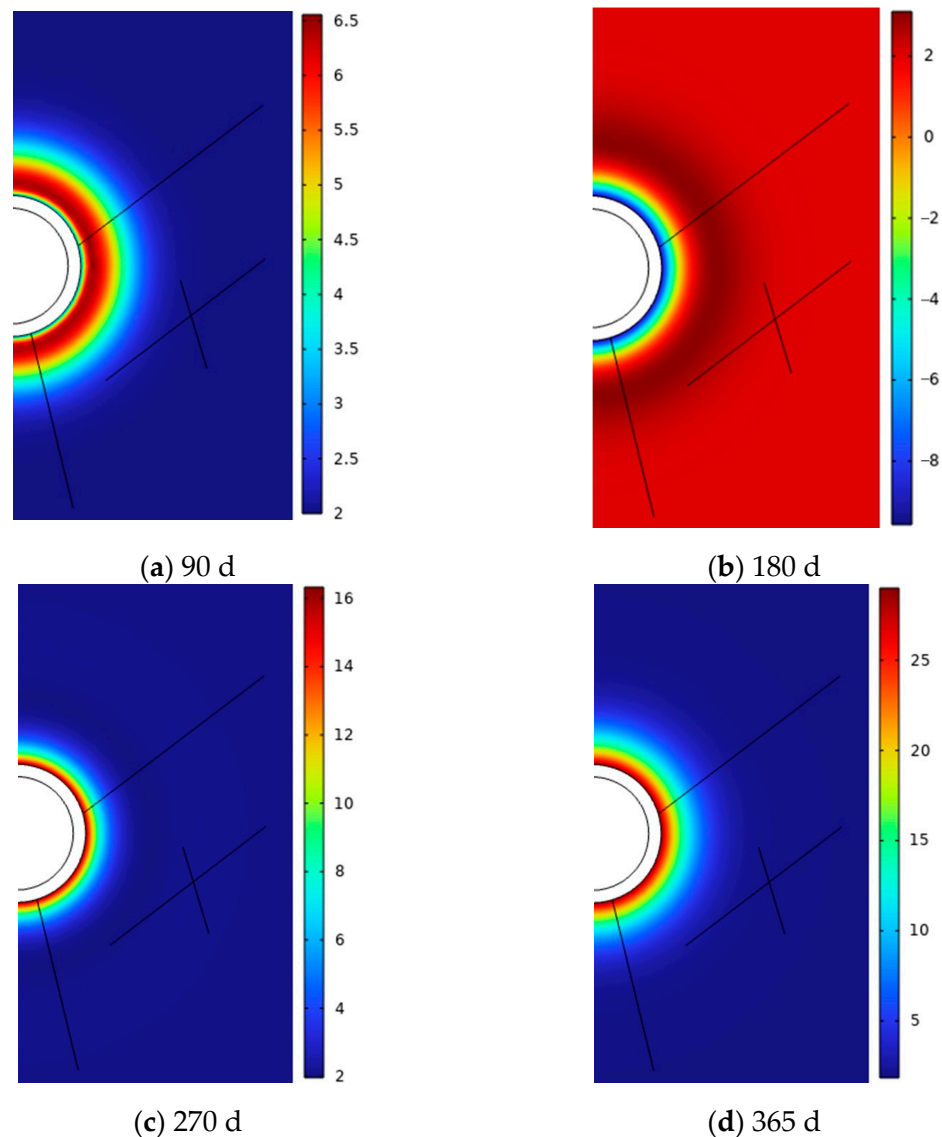
Figure 7. Cloud chart of temperature field distribution of surrounding rocks (°C).

From Figure 7, the temperature of the surrounding rock is distributed in a circular pattern. This is because the surrounding rock is set as homogeneous and isotropic material. Due to the influence of ambient temperatures, the temperature of the surrounding rock shows a trend of radial diffusion. However, by observing the cloud chart of the temperature distribution of the surrounding rock at different moments, the temperature of the surrounding rock in the radial depth of the tunnel always remains the same.
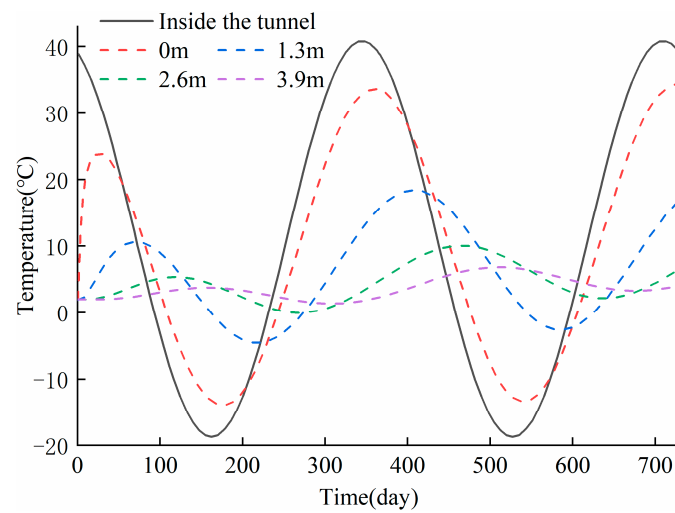
Figure 8. Temperature variation curves with time inside the tunnel and at different radial depths in the surrounding rock.

(**a**) 119 d

(**b**) 174 d
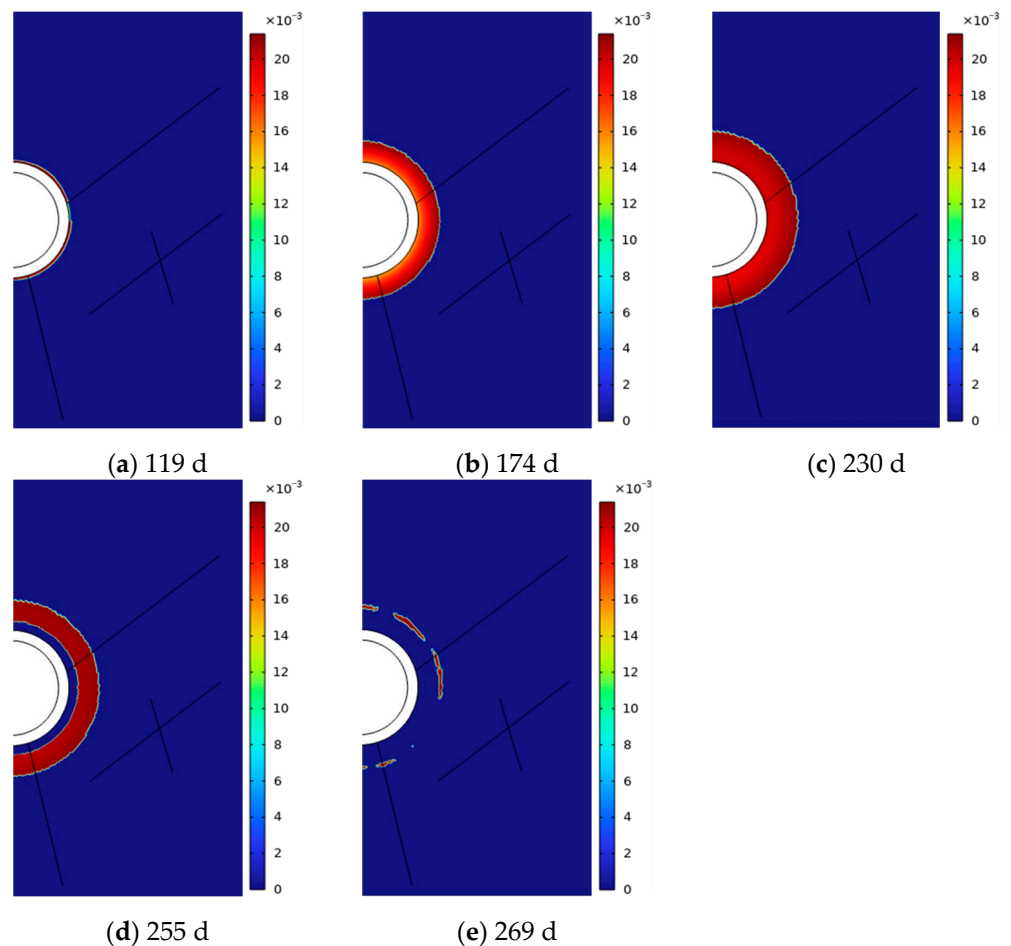
(**c**) 230 d

(**d**) 255 d

(**e**) 269 d

Figure 9. Change process of the frozen circle of surrounding rocks.

From Figure 8, it can be seen that the amplitude of the surrounding rock temperature at different radial depths in the year is different. For example, after lining, at the radial depth of 0 m of the surrounding rock, the maximum value of the temperature is 33.6 °C, the minimum value is −13.9 °C, and the amplitude is 47.5 °C; at the radial depth of 1.3 m of the surrounding rock, the maximum value of the temperature is 18.5 °C, the minimum value

is −4.6 °C, and the amplitude is 23.1 °C; at the radial depth of 2.6 m of the surrounding rock, the maximum value of the temperature is 10.1 °C, the minimum value is 0 °C, and the amplitude is 10.1 °C; and at the radial depth of 3.9 m of the surrounding rock, the maximum value of the temperature is 6.9 °C, the minimum value is 1.4 °C, and the amplitude of 5.5 °C. Since it takes time to transfer the ambient temperature to the radial depth of the tunnel-surrounding rock, the larger the radial depth of the surrounding rock, the more the temperature change in the surrounding rock will lag behind the temperature change of the surrounding rock compared with that at a smaller radial depth. For example, after lining, at the radial depth of 0 m of the surrounding rock, the first time that the temperature of the surrounding rock reaches the minimum value is at day 176; at the radial depth of 1.3 m, the first time that the temperature reaches the minimum value is at day 219; at the radial depth of 2.6 m, the first time that the temperature reaches the minimum value is at day 268; and at the radial depth of 3.9 m, the first time that the temperature reaches the minimum value is at day 307.

From Figure 9, as the ambient temperature decreases, the pore water at the cave wall first undergoes a phase change at day 119 and the surrounding rock starts to freeze. During the period when the temperature was below zero, the freezing front gradually expanded along the radial direction of the tunnel to the depths of the surrounding rock until the ambient temperature returned to above zero on the 230th day, and the freezing front no longer extended to the depths of the surrounding rock. At this time, the freezing depth of the surrounding rock behind the lining reached a maximum value of 2.6 m. Following a period of time, the surrounding rock received a positive temperature through the lining. The frozen rock at the interface between the lining and the surrounding rock began to melt, ultimately reaching a complete thaw on the 269th day.

4.3. Stress Field Analysis

After solving the distribution law of the temperature field and the moisture field in the hydraulic tunnel under large temperature differences within a year, the stress of the tunnel-surrounding rock can be calculated by using the expression of the influence of temperature and moisture on the stress within a year. The cloud chart of the maximum principal stress distribution is shown in Figure 10, and the cloud chart of the minimum principal stress distribution is shown in Figure 11.
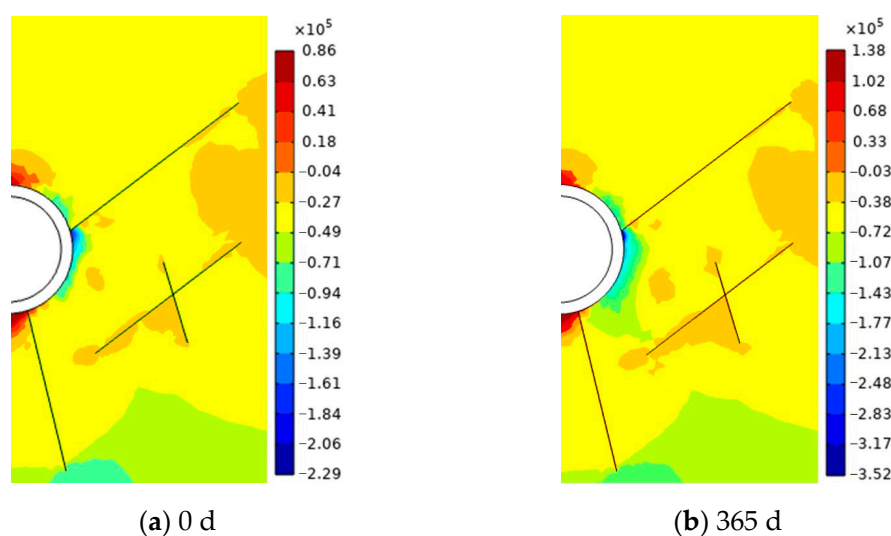

(**a**) 0 d   (**b**) 365 d

Figure 10. Cloud chart of the maximum principal stress distribution (Pa).

It can be seen from Figure 10a that the tensile stress at the cave bottom of the surrounding rock is the largest at the initial moment, and its value is 0.086 MPa. From Figure 10b, after one year of large temperature differences, the tensile stress at the cave bottom is still

the largest. Its value is 0.138 Mpa, which is 0.6 times higher than the initial moment. From Figure 11a, the compressive stress at the cave waist of the surrounding rock is the largest at the initial moment, and its value is 0.861 MPa. From Figure 11b, after one year of large temperature differences, the maximum compressive stress is still at the cave waist, and its value is 0.957 MPa, which is 11% higher than the initial moment.
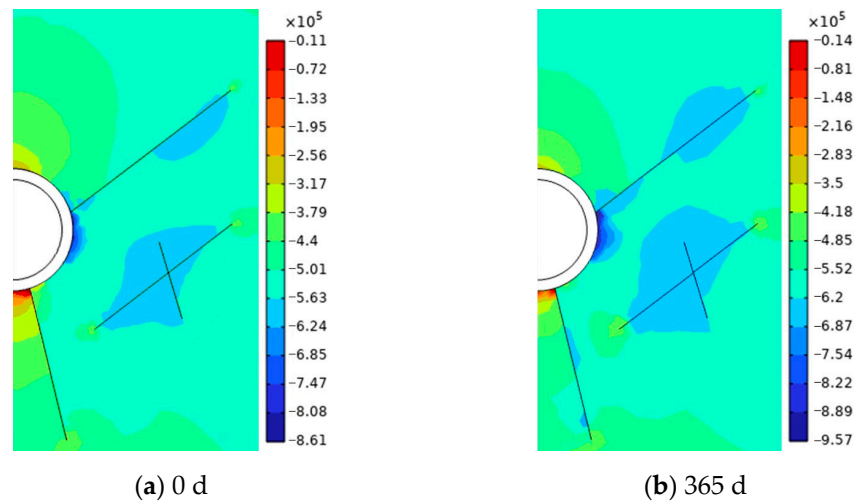

(**a**) 0 d   (**b**) 365 d

Figure 11. Cloud chart of the minimum principal stress distribution (Pa).

In addition, the changes in stress at each point over the past decade were calculated, as shown in Figure 12.
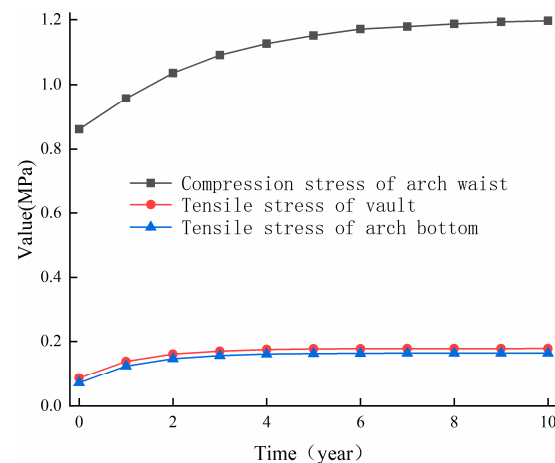

Figure 12. Changes in stress at each point over the past decade.

According to the data shown in Figure 12, the tensile stress at the cave bottom, the tensile stress at the cave top, and the compressive stress at the cave waist increased from 0.086 MPa, 0.071 MPa, and 0.861 MPa to 0.178 MPa, 0.164 MPa, and 1.197 MPa. It can be seen that all three stress values have a tendency to increase continuously during this time period. However, the growth rate does not remain constant all the time, and gradually tends to slow down with time. For example, in the first year, the growth rates of the tensile stress at the cave bottom, the tensile stress at the cave top, and the compressive stress at the cave waist are 0.052 MPa/year, 0.053 MPa/year, and 0.096 MPa/year, respectively; in the tenth year, the growth rates of the tensile stress at the cave bottom, the tensile stress at the cave top, and the compressive stress at the cave waist are 3×10^{-5} MPa/year, 4×10^{-5} MPa/year, and 0.004 MPa/year, respectively. Therefore, the tensile stress at the cave bottom and the

compressive stress at the cave waist have a tendency to increase continuously during the decade, but the growth rate tends to slow down gradually with time.

5. Conclusions

(1) Under the action of large temperature differences, the displacement of tunnel-surrounding rocks at different parts after one year is ordered as cave top > cave bottom > cave waist. The displacement sizes are 33.43 mm, 13.46 mm, and 11.81 mm, respectively. This indicates that large temperature differences have a greater influence on hydraulic tunnels. The displacement field data obtained from the calculation model established in this study are basically consistent with the measured data of a tunnel project in Xinjiang, and the displacement field changes with the same law. The reliability of the established calculation model is verified using a Mann–Whitney U test.

(2) During the time when the temperature is below zero, the freezing front gradually extends to the depth of the surrounding rock along the tunnel radial direction, and until the ambient temperature returns to zero, the freezing front will stop extending to the depth of the surrounding rock. When the ambient temperature is above zero, the frozen rock at the intersection of the lining and the surrounding rock melts first.

(3) Under the action of large temperature differences, the stress in various parts of the hydraulic tunnel-surrounding rock increases continuously. The growth rate of tensile stress at the cave bottom, the tensile stress at the cave top, and the compressive stress at the cave waist reaches 0.052 MPa/year, 0.053 Mpa/year, and 0.096 Mpa/year, respectively, in the first year, and then the increasing rate of stress tends to slow down continuously. Therefore, in actual projects, we should pay more attention to the stress growth of the tunnel-surrounding rock under the action of large temperature differences, especially the compressive stress growth at the waist of the cavern.

In the future, further research is needed on the impact of short-term large temperature differences on hydraulic tunnels.

Author Contributions: Data curation, editing, software, and analysis, P.G.; supervision and validation, S.L.; methodology, project administration, and guidance, H.J.; writing—review and editing, P.X. All authors have read and agreed to the published version of the manuscript.

Data Availability Statement: Not applicable.

Conflicts of Interest: The authors declare no conflict of interest.

References

1. Konrad, J.M.; Morgenstern, N.R. Effects of applied pressure on freezing soils. *Canadian Geotech. J.* **1982**, *19*, 494–505. [CrossRef]
2. Yu, Y.; Tang, L.; Ling, X.Z.; Geng, L.; Wei, S.W.; Zhou, G.Q. Investigation of the soil-lining interaction at a tunnel entrance during freeze-thaw cycling: Model testing and semi-empirical modeling. *Tunn. Undergr. Space Technol.* **2021**, *115*, 104028. [CrossRef]
3. Zhang, Y.Q.; Yang, P.; Li, L.; Zhang, T. Characterizing Influence of Salt and Freeze–Thaw Cycle on Strength Properties of Clay. *Int. J. Appl. Mech.* **2022**, *14*, 2250045. [CrossRef]
4. Xu, P.; Wu, Y.M.; Wang, Z.J.; Huang, L. Distribution laws of freeze-thaw cycles and unsaturated concrete experiments in cold-region tunnels. *Cold Reg. Sci. Technol.* **2020**, *172*, 102985. [CrossRef]
5. Moon, J.S.; An, J.W.; Kim, H.K.; Lee, J.G.; Lattner, T. Evaluation criteria for freezing and thawing of tunnel concrete lining according to theoretical and experimental analysis. *Geomech. Eng.* **2022**, *29*, 349–357. [CrossRef]
6. Sardana, S.; Sinha, R.K.; Verma, A.; Jaswal, M.; Singh, T.N. Influence of freeze–thaw on the stability of road cut slopes—A case study in the Indian Himalayan region. *Can. Geotech. J.* **2022**, *60*, 107–112. [CrossRef]
7. Yao, X.C.; Li, N.; Wan, K.C.; Lv, G.; He, M.M. Experimental and analytical study on mechanical properties of high rock temperature diversion tunnel. *Adv. Civ. Eng.* **2019**, *2019*, 9537153. [CrossRef]
8. Li, A.G.; Gao, X.P.; Ren, T. Study on thermal pressure in a sloping underground tunnel under natural ventilation. *Energy Build.* **2017**, *147*, 200–209. [CrossRef]

9.   Nakano, Y. Quasi-steady problems in freezing soils: I. Analysis on the steady growth of an ice layer. *Cold Reg. Sci. Technol.* **1990**, *17*, 207–226. [CrossRef]

10.   Gatmiri, B.; Delage, P. A formulation of fully coupled thermal–hydraulic–mechanical behaviour of saturated porous media—Numerical approach. *Int. J. Numer. Anal. Methods Geomech.* **1997**, *21*, 199–225. [CrossRef]

11.   Zhu, T.T.; Su, Z.M.; Li, A.; Huang, D.; Zong, X.L.; Ma, F.W. Study of the evolution of the frost–heaving pressure of a tunnel lining based on a constant stiffness constraint model. *Cold Reg. Sci. Technol.* **2022**, *202*, 103644. [CrossRef]

12.   Liu, C.L.; Zhang, Y.S.; Yuan, J.G.; Zhong, Y.; Zhang, Y. Study on the Distribution of Stress Field in High-temperature Diversion Tunnels. *J. Water Resour. Archit. Eng.* **2015**, *13*, 66–71. [CrossRef]

13.   Dong, F.; Dong, Y. Selection of wall rock thickness for thermal stress analysis of circular tunnel concrete lining. *J. Eng. Mech.* **2013**, *139*, 916–919. [CrossRef]

14.   Deng, S.J.; Chen, H.L.; Gong, X.N.; Zhou, J.J.; Hu, X.D.; Jiang, G. A Frost Heaving Prediction Approach for Ground Uplift Simulation Due to Freeze-Sealing Pipe Roof Method. *Cmes-Comput. Model. Eng. Sci.* **2022**, *132*, 251–266. [CrossRef]

15.   Bonacina, C.; Comini, G.; Fasano, A.; Primicerio, M. Numerical solution of phase-change problems. *Int. J. Heat Mass Transf.* **1973**, *16*, 1825–1832. [CrossRef]

16.   Zhang, J.M.; Guo, L. Peridynamics simulation of shotcrete lining damage characteristics under freeze-thaw cycles in cold region tunnels. *Eng. Anal. Bound. Elem.* **2022**, *141*, 17–35. [CrossRef]

17.   Yu, Q.Y.; Lei, P.; Dai, Z.X.; Soltanian, M.R.; Yin, S.X.; Liu, W.; Xiong, Z.W. Damage Characteristics of Limestone under Freeze–Thaw Cycle for Tunnels in Seasonal Frozen Areas. *Iran. J. Sci. Technol. Trans. Civ. Eng.* **2023**, *47*, 469–477. [CrossRef]

18.   Liu, H.Y.; Yuan, X.P.; Xie, T.C. A damage model for frost heaving pressure in circular rock tunnel under freezing-thawing cycles. *Tunn. Undergr. Space Technol.* **2019**, *83*, 401–408. [CrossRef]

19.   Kang, Y.S.; Liu, Q.S.; Huang, S.B. A fully coupled thermo-hydro-mechanical model for rock mass under freezing/thawing condition. *Cold Reg. Sci. Technol.* **2013**, *95*, 19–26. [CrossRef]

20.   Hao, S.J.; Fei, R.Z. Optimisation Study on Crack Resistance of Tunnel Lining Concrete Under High Ground Temperature Environment. *Geotech. Geol. Eng.* **2022**, *40*, 3985–4006. [CrossRef]

21.   Zhao, Z.H.; Xu, H.R.; Liu, G.H.; Liu, F.; Wang, G.L. A robust numerical method for modeling ventilation through long tunnels in high temperature regions based on 1D pipe model. *Tunn. Undergr. Space Technol.* **2021**, *115*, 104050. [CrossRef]

22.   Zeng, Y.H.; Tao, L.L.; Ye, X.Q.; Zhou, X.H.; Fang, Y.; Fan, L.; Liu, X.R.; Yang, Z.X. Temperature reduction for extra-long railway tunnel with high geotemperature by longitudinal ventilation. *Tunn. Undergr. Space Technol.* **2020**, *99*, 103381. [CrossRef]

23.   Che, Q. Numerical Simulation of Thermal Environment in High Heat Tunnel. In Proceedings of the Advanced Materials Research, San Francisco, CA, USA, 9–13 April 2012; pp. 519–523. [CrossRef]

24.   Wu, D.; Zhang, Y.L.; Zhao, R.K.; Deng, T.F.; Zheng, Z.X. A coupled thermal-hydraulic-mechanical application for subway tunnel. *Comput. Geotech.* **2017**, *84*, 174–182. [CrossRef]

25.   Liu, Y.; Yang, B.; Cheng, H.; Zhou, Q.J.; Zhang, G.X.; Zhang, X.S.; Li, H.T. Study on the Influence of Severe Cold and High Temperature Differences on the Working Behavior of High Arch Dams and the Preliminary Solution. *Water Power* **2021**, *47*, 37–44. [CrossRef]

26.   Zhang, H.; Hao, J.Q. Mechanized Construction Technology of Cast-in-place Concrete Lining of Channel Slope Under of Drought and Large Temperature Difference. *Road Mach. Constr. Mech.* **2016**, *33*, 81–83. [CrossRef]

27.   Wang, H.H. *Heat Transfer*; Chongqing University Press: Chongqing, China, 2006; pp. 11–22.

28.   Bai, Q.B. *Determination of Boundary Layer Parameters and a Preliminary Research on Hydrothermal Stability of Subgrade in Cold Region*; Beijing Jiaotong University: Beijing, China, 2016. [CrossRef]

29.   Lu, N.; Likos, W.J. *Unsaturated Soil Mechanics*; Higher Education Press: Beijing, China, 2012; pp. 106–109.

30.   Taylor, G.S.; Luthin, J.N. A model for coupled heat and moisture transfer during soil freezing. *Can. Geotech. J.* **1978**, *15*, 548–555. [CrossRef]

31.   Mann, H.B.; Whitney, D.R. On a test of whether one of two random variables is stochastically larger than the other. *Ann. Math. Stat.* **1947**, *18*, 50–60. [CrossRef]